How to cite: *Angew. Chem. Int. Ed.* **2022,** *61,* e202209486
International Edition: doi.org/10.1002/anie.202209486
German Edition: doi.org/10.1002/ange.202209486

Hydrogen Evolution

Competitive Adsorption: Reducing the Poisoning Effect of Adsorbed Hydroxyl on Ru Single-Atom Site with SnO_2 for Efficient Hydrogen Evolution

Jiachen Zhang, Guangbo Chen, Qicheng Liu, Chuang Fan, Dongmei Sun, Yawen Tang, Hanjun Sun, and Xinliang Feng**

Abstract: Ruthenium (Ru) has been theoretically considered a viable alkaline hydrogen evolution reaction electrocatalyst due to its fast water dissociation kinetics. However, its strong affinity to the adsorbed hydroxyl (OH_{ad}) blocks the active sites, resulting in unsatisfactory performance during the practical HER process. Here, we first reported a competitive adsorption strategy for the construction of SnO_2 nanoparticles doped with Ru single-atoms supported on carbon (Ru SAs-SnO_2/C) via atomic galvanic replacement. SnO_2 was introduced to regulate the strong interaction between Ru and OH_{ad} by the competitive adsorption of OH_{ad} between Ru and SnO_2, which alleviated the poisoning of Ru sites. As a consequence, the Ru SAs-SnO_2/C exhibited a low overpotential at 10 mA cm^{-2} (10 mV) and a low Tafel slope of 25 mV dec^{-1}. This approach provides a new avenue to modulate the adsorption strength of active sites and intermediates, which paves the way for the development of highly active electrocatalysts.

Introduction

Electrochemical hydrogen evolution reaction (HER) under alkaline conditions has been regarded as an economical route to produce sustainable green hydrogen energy without reliance on traditional fossil fuels.[1] Under alkaline conditions, the HER performance of the electrocatalyst is determined by the prior water dissociation process (Volmer step) and the subsequent hydrogen combination process (Heyrovsky or Tafel step). To overcome the sluggish kinetics during the alkaline HER process, most reported alkaline HER catalysts mainly focused on optimizing the dissociation energy of water and the adsorption energy of H.[2] However, the influence of adsorbed hydroxyl (OH_{ad}) on active sites has been paid less attention. Principally, the Volmer step ($H_2O + e^- \rightleftharpoons H_{ad} + OH^-$) can be divided into $H_2O \rightleftharpoons H_{ad} + OH_{ad}$ and $OH_{ad} + e^- \rightleftharpoons OH^-$.[3] ($H_{ad}$: the adsorbed hydrogen atom). The strong binding energy between active sites and OH_{ad} inhibits the OH_{ad} transfer process during the Volmer reaction and limits its overall HER activity.[4] Therefore, rational design of HER electrocatalysts to alleviate the strong adsorption between active sites and OH_{ad} is essential.

As a member of Pt-group metals, Ru has been proved to be an ideal substitute for catalyzing the HER due to the following reasons: (1) Ru possesses a relatively low price, about one-third that of Pt,[5] (2) Ru has high efficiency on water dissociation, which accelerates the rate of the Volmer reaction and facilitates the proton supply for the subsequent reaction,[2a,4a,6] (3) the strong metal-hydrogen (Ru–H) bonds lead to a rapid H-adsorption.[5,7] Despite the above advantages of Ru, its performance during practical alkaline HER is not satisfactory: based on Brønsted–Evans–Polanyi (BEP) principles, a low H_2O-dissociation barrier leads to the strong adsorption of H_{ad}/OH_{ad} on the surface.[2a,8] Although the strong interaction between Ru and H atoms is beneficial to the H-adsorption, it impedes the efficiency of H-desorption.[6,9] More importantly, the strong Ru-OH_{ad} binding energy leads to the poisoning of Ru active sites required for re-adsorption of water, which decreases the efficiency OH_{ad} transfer process, the rate-determining step during the Volmer reaction and slows down the rate of HER.[4] Up to now, many efforts have been devoted to developing Ru-based HER catalysts by optimizing the strong hydrogen adsorption between Ru and H (e.g. RuAu single-atom alloy,[6] CoRu/CQDs[9a]), which accelerates H-desorption.

[*] J. Zhang, Q. Liu, C. Fan, Prof. D. Sun, Prof. Y. Tang, Prof. H. Sun
Jiangsu Key Laboratory of New Power Batteries, Jiangsu Collaborative Innovation Centre of Biomedical Functional Materials, School of Chemistry and Materials Science, Nanjing Normal University
1 Wenyuan Road, Nanjing 210023 (China)
E-mail: hanjun.sun@njnu.edu.cn
Dr. G. Chen, Prof. X. Feng
Center for Advancing Electronics Dresden (cfaed) and Faculty of Chemistry and Food Chemistry, Technische Universität Dresden
Mommsenstr. 4, 01062 Dresden (Germany)
E-mail: xinliang.feng@tu-dresden.de
Prof. X. Feng
Department of Synthetic Materials and Functional Devices, Max Planck Institute of Microstructure Physics
Weinberg 2, Halle (Saale) (Germany)

Nevertheless, the design of Ru-based electrocatalysts by reducing the strong adsorption between Ru and OH_{ad} has not attracted attention.

Herein, we demonstrated the synthesis of SnO_2 nanoparticles doped with Ru single-atoms supported on carbon (Ru SAs-SnO_2/C) as a novel electrocatalyst to regulate the strong interaction between Ru and OH_{ad}. For the first time, we attempted to introduce SnO_2 (an oxophilic species, that owned excellent adsorption capability of OH_{ad}) to alleviate the poisoning of OH_{ad} on Ru sites by the competitive adsorption of OH_{ad} between Ru and SnO_2. Since OH_{ad} is adsorbed preferentially on SnO_2, the OH_{ad} transfer process ($OH_{ad}+e^- \rightleftharpoons OH^-$, the key step of Vomer reaction) and the regeneration of Ru active sites are effectively facilitated. As such, the as-prepared Ru SAs-SnO_2/C catalyst exhibited a low overpotential at 10 mA cm^{-2} (10 mV), a low Tafel slope of 25 mV dec^{-1}, and an ultrahigh turnover frequency (TOF) value of 5.44 H_2 s^{-1} at 100 mV in 1.0 M KOH electrolyte, which was much lower than those of commercial Pt/C (21 mV at 10 mA cm^{-2}, Tafel slope of 32 mV dec^{-1}, 0.74 H_2 s^{-1}). In addition, the mass activity of Ru SAs-SnO_2/C at 25 mV was about 8.2 times higher than that of Pt/C, indicating a higher utilization of noble metals. Moreover, this performance was also superior to that of other recently reported Pt-based and Ru-based HER electrocatalysts.[10] Combined with density functional theory (DFT), our results elucidated that the introduction of SnO_2 reduced the OH_{ad} poisoning effect on Ru sites, which overcame the efficiency loss in the Volmer step.

Results and Discussion

Material Synthesis and Characterization

Figure 1 presents the synthetic procedure of Ru SAs-SnO_2/C, which was prepared using XC-72 Vulcan carbon (40 mg), $RuCl_3{\cdot}xH_2O$ (0.1 mmol), and $SnCl_2{\cdot}2H_2O$ (0.15 mmol) as raw materials (see the details in the Supporting Information). After mixing Ru ions, Sn ions and activated carbon in the aqueous solution, the pH was adjusted to 1.3 to avoid the hydrolysis of Sn^{2+} (Note 1, Supporting Information). After annealing at 300 °C in N_2 atmosphere to improve the crystallization, the $RuSnO_2$/C-0.1 (denoted as Ru SAs-SnO_2/C) with a Ru content of 3.99 wt % was obtained. The SnO_2 offered isolated sites on the surface for the formation of Ru single atoms, which could be attributed to the atomically galvanic replacement between Sn^{2+} and Ru^{3+} (oxidation-reduction potential: $\phi Ru^{3+}/Ru = 0.39$ V; $\phi Ru^{3+}/Ru^{2+} = 0.26$ V vs. $\phi Sn^{4+}/Sn^{2+} = 0.15$ V). Thus, Ru^{3+} could be reduced by Sn^{2+}, and Sn^{2+} was converted to Sn^{4+}. Meanwhile, the Sn^{4+} can be converted to SnO_2 due to its hydrolysis at pH 1.3 (Note 2, Supporting Information; Figure S1, Supporting Information). The formation of Ru–O single atoms is mostly due to the Ru–O was thermodynamically more stable than Ru–Ru in this system because of its more stable structure (Ru–O: R(Å) = 2.09 Å; Ru–Ru: R-(Å) = 2.68 Å). In addition, the unsaturated sites on the surface of SnO_2 functioned as the supporting materials for anchoring single Ru atoms and promoted the formation of Ru single atoms.[11] Additionally, the activated carbon functioned as support to disperse SnO_2 nanoparticles (average size: 2.0 nm, Figure S2, Supporting Information) and enhanced the conductivity of electrocatalyst. The lattice fringe with a spacing of 0.348 nm was determined by high-resolution transmission electron microscopy (HRTEM), which corresponded to the (110) plane of SnO_2. Energy dispersive spectrometer (EDS) elemental mapping analysis indicated that Ru and Sn atoms were distributed evenly throughout the particle (Figure 2c–f), which further confirmed the uniform distribution of Ru in SnO_2 nanoparticles on the carbon. In addition, high-angle annular dark field-scanning transmission electron microscopy (HAADF-STEM) analysis gave more details on the structure informa-

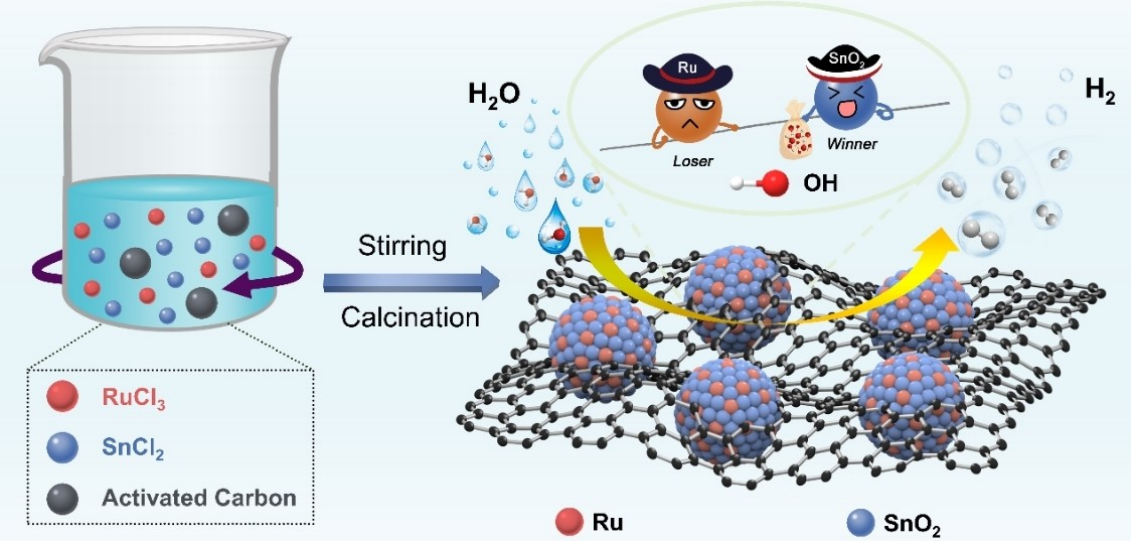

Figure 1. Synthesis scheme of Ru SAs-SnO_2/C.

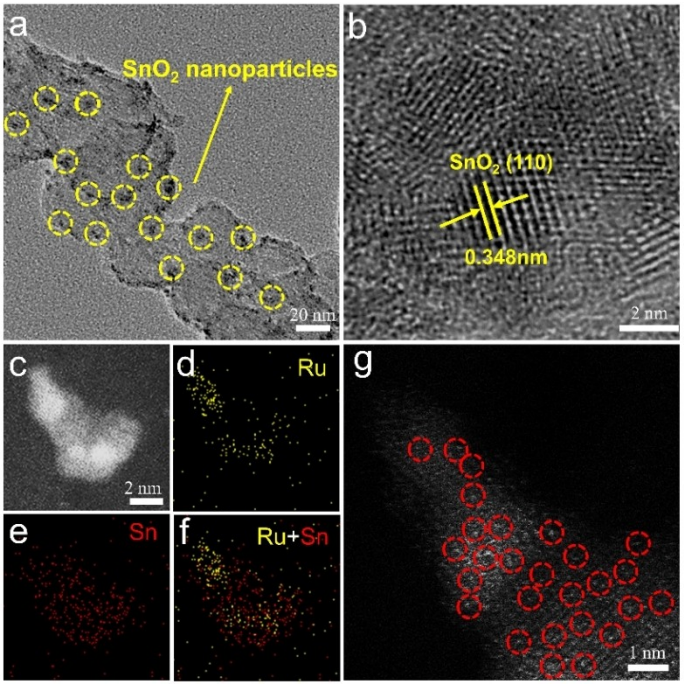

Figure 2. a) TEM image of Ru SAs-SnO_2/C. b) HRTEM image of Ru SAs-SnO_2/C. c) Low-resolution HAADF-STEM images of Ru SAs-SnO_2/C, and related EDX elemental mapping images of d) Ru, e) Sn and f) Ru + Sn. g) Atomic-resolution HAADF-STEM image of Ru SAs-SnO_2/C, Ru atoms (marked by red circles) are uniformly distributed through the nanoparticles.

tion about Ru SAs-SnO_2/C. As shown in Figure 2g, although abundant bright dots (in red circles) could be seen on the surface of SnO_2, it was difficult to distinguish whether it was Ru or Sn because the relative atomic mass of Sn was similar with that of Ru (Ru: 101.1, Sn: 118.7). Thus, X-ray absorption spectroscopy (XAS) was further employed to investigate the electronic structure and coordination environment of Ru. The crystal structures of Ru SAs-SnO_2/C and SnO_2/C were then investigated by X-ray diffraction (XRD). As shown in Figures S3–S4 (Supporting Information), the peak at around 26.6, 33.9, 42.6, 51.8, and 64.8 could be assigned to the characteristic (110), (101), (210), (211) and (112) fact of SnO_2, respectively (JCPDS 41-1445). No diffraction peaks related to Ru species were detected, indicating that the Ru species Ru SAs-SnO_2/C were amorphous or atomically dispersed.[12]

In addition, Ru-SnO_2/C catalysts with different Ru content (0.025 mmol, 0.15 mmol, 0.25 mmol and 0.4 mmol) were also prepared, and the corresponding products were denoted as Ru-SnO_2/C-0.025, Ru-SnO_2/C-0.15, Ru-SnO_2/C-0.25 and Ru-SnO_2/C-0.4. With the increasing of Ru content, aggregated Ru nanoclusters without lattice stripes can be found on the surface of SnO_2 (Figures S5–S9, Supporting Information). All the samples exhibited similar diffraction patterns as Ru SAs-SnO_2/C (Figure S10, Supporting Information), manifesting that the varying inventories of Ru precursor during preparation process didn't change the crystal structure of Ru species (Table S1, Supporting Information). While for RuSnO_2/C-0.25 and RuSnO_2/C-0.4, the content of Ru was almost the same (an upper limit, 9.75 wt %).

Fourier transform infrared spectroscopy analysis revealed that wavenumber at 561 cm^{-1} corresponds to metal-O, which can be attributed to the Sn–O or Ru–O stretching vibration (Figure S11; Supporting Information).[13] X-ray photoelectron spectroscopy (XPS) was performed to gain insights into the chemical composition of Ru SAs-SnO_2/C. As depicted in Figure S12 (Supporting Information), the survey spectrum confirmed the presence of Ru, Sn, O, and C elements in Ru SAs-SnO_2/C. Meanwhile, the O 1s spectra can be deconvoluted into three peaks, the binding energies located at 531.0, 531.8 and 532.9 eV, corresponding to Sn (Ru)–O, C–O–C configuration and physically/chemically adsorbed water species, respectively.[1c] In addition, the XPS of RuSnO_2/C catalysts with different Ru content was also measured (Figure S13; Supporting Information). The results showed that all the samples owned similar characteristic peaks of Sn 3d. Meanwhile, the binding energies of Ru $3p_{3/2}$ in all RuSnO_2/C catalysts were between Ru^{IV} and Ru^0, which demonstrated that the oxidation state of Ru in RuSnO_2/C was between Ru^{4+} and Ru^0.[14] Based on the above results, it is reasonable to conclude that metallic Ru and RuO_2 are not present in Ru SAs-SnO_2/C, and Ru atoms was coordinated with the O atoms in SnO_2 nanoparticles.

To further investigate the electronic structure and coordination environment of Ru SAs-SnO_2/C, X-ray absorption spectroscopy (XAS) was employed (Figure 3a). The partially enlarged illustration (Figure 3b) showed the threshold value (E_0) of Ru SAs-SnO_2/C (22125 eV) was between Ru foil (22117 eV) and RuO_2 (22130 eV), suggesting the transition energy from 1 s to the outermost shell orbitals in these three samples increased in the order: Ru foil < Ru

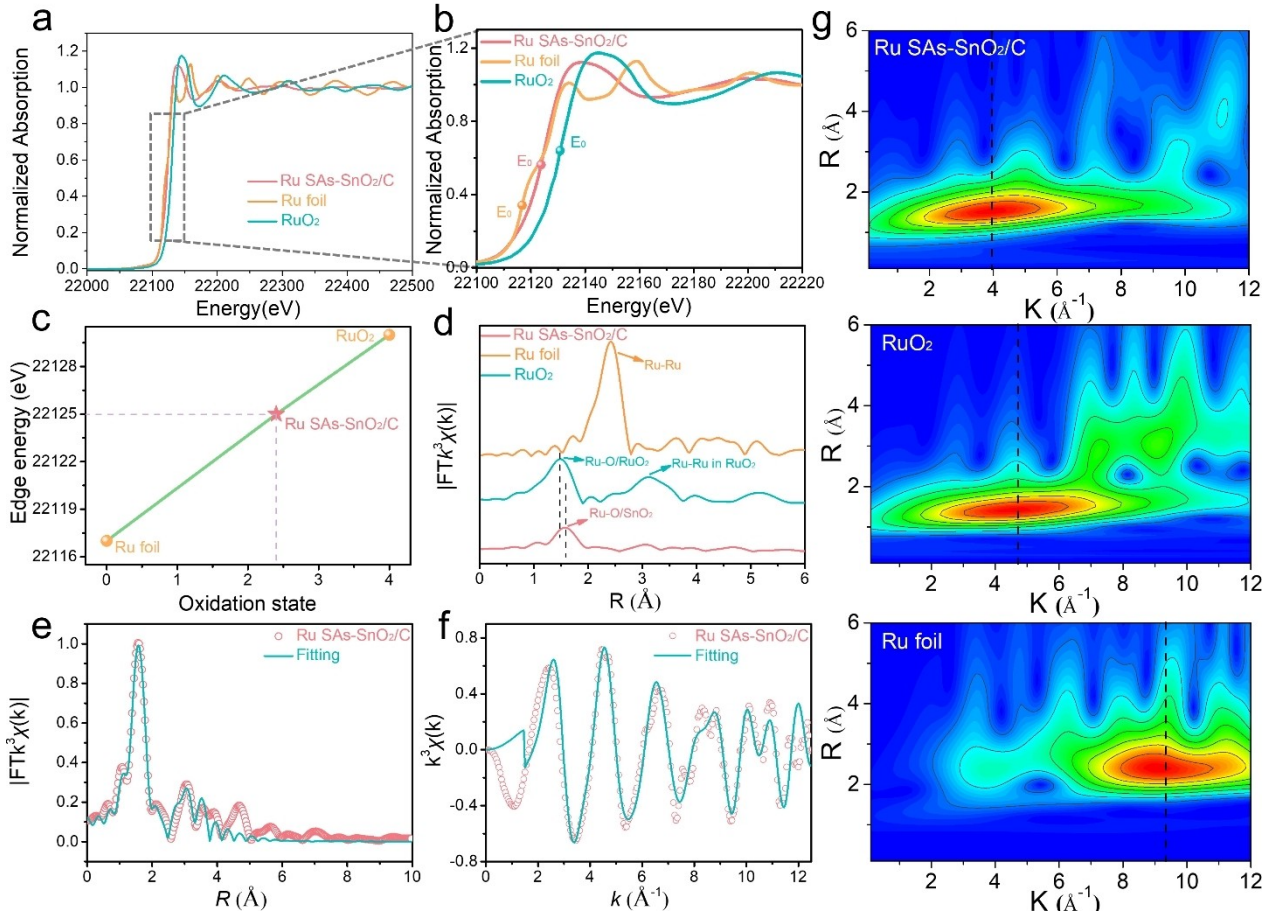

Figure 3. a) Ru *k*-edge XANES spectra of Ru SAs-SnO_2/C, Ru foil, and RuO_2. b) Ru *k*-edge with different absorption energy (E_0) for Ru SAs-SnO_2/C, Ru foil and RuO_2, respectively. c) Relationship between Ru *k*-edge absorption energy (E_0) and oxidation state for Ru SAs-SnO_2/C, Ru foil and RuO_2. d) Fourier-transformed Ru *k*-edge EXAFS spectra of Ru SAs-SnO_2/C, Ru foil and RuO_2. e) EXAFS fitting curves of Ru SAs-SnO_2/C at the *R* space. f) EXAFS fitting curves of Ru SAs-SnO_2/C at the *K* space. g) Wavelet transforms for the k^3-weighted Ru *k*-edge EXAFS signals of Ru SAs-SnO_2/C, Ru foil, and RuO_2.

SAs-SnO_2/C < RuO_2.[15] For further evaluating the oxidation state of Ru in Ru SAs-SnO_2/C, E_0 was used as the function of oxidation state of Ru in these three materials.[16] Hence, further fitting (Figure 3c) indicated that the average oxidation state of Ru was +2.4. Fourier transformed k^3-weighted $\chi(k)$-function of extended X-ray absorption fine structure (EXAFS) spectrum for Ru SAs-SnO_2/C displayed that there was a characteristic peak around 1.58 Å (Figure 3d), suggesting that the peak was associated with the backscattering between Ru and light atoms (O),[17] which is consistent with the XPS results. However, the characteristic peak value was larger than that of RuO_2 (1.47 Å). Meanwhile, another characteristic peak (3.12 Å) for RuO_2 was not observed in the EXAFS spectrum of Ru SAs-SnO_2/C, demonstrating the absence of RuO_2 in Ru SAs-SnO_2/C.[14a,17] Besides, no characteristic peak corresponding to the Ru–Ru bond was detected in the EXAFS spectrum of Ru SAs-SnO_2/C. The above results indicated that Ru existed in the form of isolated atoms. Then, quantitative EXAFS curve-fitting analysis for Ru SAs-SnO_2/C was carried out to reveal the coordination number of Ru SAs-SnO_2/C.[12] As shown in Figure 3e–f and Table S2, the coordination number of the Ru–O bonding shell was 2.9, confirming that each Ru atom was coordinated with ≈3 oxygen atoms. Quantitative EXAFS curve-fitting analysis (Figure 3e–f, Figure S14, Table S2, Supporting Information) of Ru SAs-SnO_2/C showed that the bond length of Ru–O was 2.09 Å. The shorter bond length of Ru–O than that of Ru–Ru (2.68 Å) indicated that the Ru SAs coordinated with O atoms are much more stable than those of Ru–Ru bond thermodynamically, which also explained that why Ru reduced to isolated Ru–O sites on the surface of SnO_2 nanoparticles rather than Ru^0 clusters.

The resolution in *k* space and radial distance resolution can be displayed by wavelet transforms (WT) of EXAFS at the same time (Figure 3g).[7] A strong signal was observed at 3.9 Å, which was attributed to the coordination contribution between Ru and O atoms. Meanwhile, no intensity maximum at 9.3 Å associated with the Ru–Ru bond was detected in Ru SAs-SnO_2/C, further confirming that Ru atoms were atomically dispersed in the Ru SAs-SnO_2/C. Together with the XRD pattern and XPS spectra on the microstructure of Ru SAs-SnO_2/C, it was clear that SnO_2 nanoparticles doped with Ru single-atom was successfully synthesized in this work.

HER Performance

To evaluate the HER performance of Ru SAs-SnO_2/C, a typical three-electrode system in N_2-saturated 1.0 M KOH solution was applied using a Hg/HgO electrode and a graphite rod as the reference and counter electrodes, respectively. The linear sweep voltammetry (LSV) curves were iR-corrected in this work and the all the potentials were referenced to the reversible hydrogen electrode (RHE) (Figure S15, Supporting Information). For comparison, the HER performance of commercial Ru/C (5 %), Pt/C (20 %), and SnO_2/C were also measured under the same test conditions. Remarkably, the Ru SAs-SnO_2/C exhibited almost a zero-onset potential for HER. Moreover, the Ru SAs-SnO_2/C achieved a current density of 10 mA cm^{-2} at an overpotential of only 10 mV, being 11 mV and 64 mV lower than that of the commercial Pt/C and Ru/C (Figure 4a). Figure S16 (Supporting Information) indicated that there was an optimal value of Ru content. With the increase of Ru content, the activity of Ru SAs-SnO_2/C ($RuSnO_2$/C-0.1) was superior to that of the $RuSnO_2$/C-0.025 owing to the formation of more Ru active sites. However, with the further increase of Ru content, the activity of the Ru-SnO_2/C catalyst decreased, which can be attributed to the formation of aggregated Ru clusters. The double layer capacitances (C_{dl}) of Ru SAs-SnO_2/C and Ru/C were also investigated, which was generally proportional to the electrochemical surface areas (ECSA). As presented in Figure S17 (Supporting Information), the value of C_{dl} for Ru SAs-SnO_2/C was 21.2 mF cm^{-2}, which was much higher than that of Ru/C (5.3 mF cm^{-2}) and SnO_2/C (4.5 mF cm^{-2}). These results indicated that more catalytically active sites were exposed on the surface of Ru SAs-SnO_2/C, increasing the utilization of Ru and further enhancing HER activity.

As shown in Figure 4b, such outstanding HER performance of Ru SAs-SnO_2/C was also demonstrated through its Tafel slope (25 mV decade^{-1}), which was much lower than that of commercial Pt/C (32 mV decade^{-1}) and Ru/C (68 mV decade^{-1}). Even when compared with the previously reported Pt-based and Ru-based HER electrocatalysts in 1.0 M KOH, the small overpotential of Ru SAs-SnO_2/C at 10 mA cm^{-2} also displayed a greater advantage for HER (Figure 4c; Table S3, Supporting Information), such as Pt-PVP/TiO_2@graphitic carbon (≈21 mV at 10 mA cm^{-2}),[10b] $PtSe_2$/Pt (≈42 mV at 10 mA cm^{-2}),[10a] Ru@C_2N (≈17 mV at 10 mA cm^{-2}),[4a] $CoRu_{0.5}$/carbon quantum dots (≈18 mV at 10 mA cm^{-2}),[9a] $NiRu_{0.13}$-BDC (≈36 mV at 10 mA cm^{-2}),[1c] Ni_5P_4-Ru (≈54 mV at 10 mA cm^{-2}).[12] Meanwhile, the exchange current density (J_0) of Ru SAs-SnO_2/C (6.58 mA cm^{-2}) can be evaluated by extrapolating the Tafel plots (Figure S18; Supporting Information), which was much higher than those of commercial Pt/C (4.96 mA cm^{-2}) and Ru/C (1.50 mA cm^{-2}), indicating rapid electron transfer rate between electrode and catalyst surface. To evaluate the intrinsic HER performance of electrocatalysts, the turnover frequency (TOF) was calculated. The TOF values of Ru SAs-SnO_2/C and Pt/C based on the estimated numbers of the active sites, along with other those of recently reported HER catalysts in alkaline solution are shown in Figure S19 (Supporting Information). The TOF value of Ru SAs-SnO_2/C was 12.44 H_2 s^{-1} at −50 mV, which was 2.66 times higher than that of Pt/C (4.68 H_2 s^{-1}), and even far beyond most

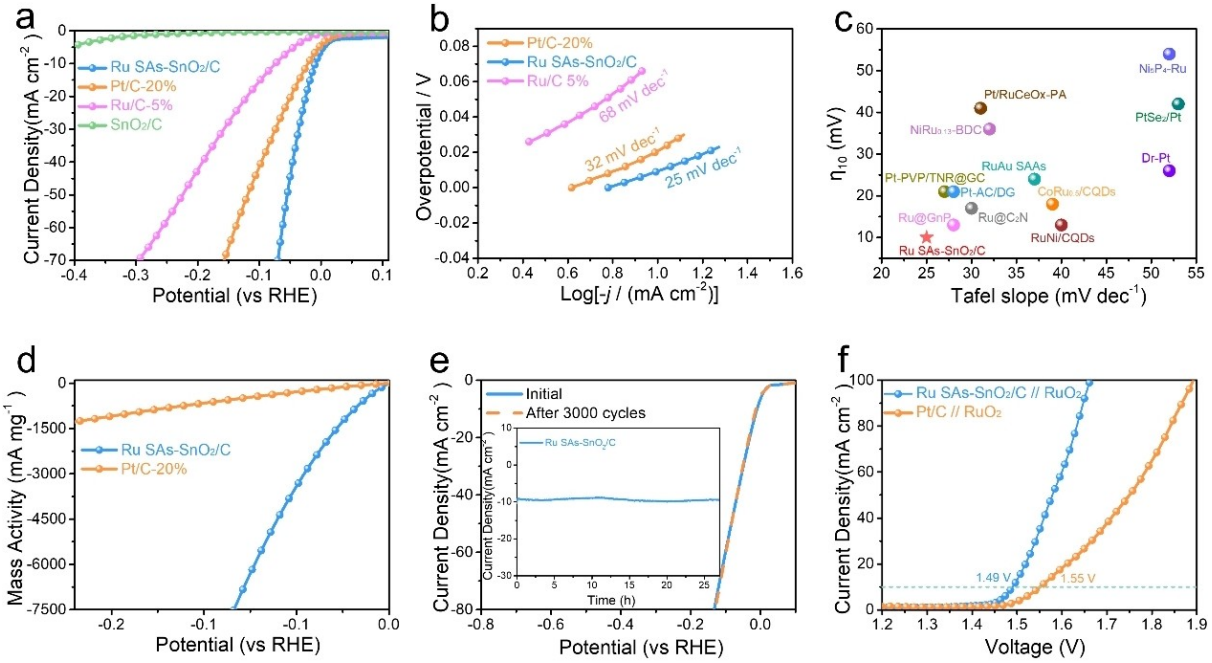

Figure 4. a) LSV curves (iR compensated) and b) the related Tafel plots of Ru SAs-SnO_2/C, Ru/C, Pt/C, and SnO_2/C electrocatalysts in 1.0 M KOH at a scan rate of 5 mV s^{-1}. c) Comparison with the recently reported Ru-based HER electrocatalysts in 1.0 M KOH. d) Mass activity of Ru SAs-SnO_2/C and Pt/C. e) LSV curves of Ru SAs-SnO_2/C electrocatalyst before and after 3000 CV cycles. The inset illustrates the chronoamperometry curve at −0.018 V. f) Polarization curves of the Ru SAs-SnO_2/C||RuO_2 and Pt/C||RuO_2 electrolyzers for overall water splitting.

reported Ru-based HER electrocatalysts (Table S4, Supporting Information), including Ru@multi-walled carbon nanotubes (0.40 $H_2 s^{-1}$ at −25 mV),[5] Ru@C_2N (0.76 $H_2 s^{-1}$ at −25 mV),[4a] RuAu single-atom alloy (2.18 $H_2 s^{-1}$ at −50 mV),[6] RuNi/CQDs (5.03 $H_2 s^{-1}$ at −100 mV),[1a] Ru/C_3N_4/C (4.2 $H_2 s^{-1}$ at −100 mV),[9c] Ru/Co@ carbon quantum dot hybrid (6.2 $H_2 s^{-1}$ at −100 mV),[18] and R-NiRu (0.78 $H_2 s^{-1}$ at −100 mV).[13] The above results indicated the Ru SAs-SnO_2/C exhibited higher intrinsic HER activity. Considering the cost of catalysts for practical application, the mass activity of Ru SAs-SnO_2/C and commercial Pt/C were evaluated by normalizing the LSV curves based on the masses of Pt and Ru, respectively. As shown in Figure 4d, the mass activity of Ru SAs-SnO_2/C at −25 mV was 1262.7 $mA mg^{-1}_{Ru}$, about 8.2 times higher than that of Pt/C (122.4 $mA mg^{-1}_{Pt}$), implying greater superiority for practical application.

Stability is another important parameter to evaluate the practical application of electrocatalysts. Here, a long-term cycling test was also carried out to evaluate the electrocatalytic stability of Ru SAs-SnO_2/C. As shown in Figure 4e, the polarization curves of Ru SAs-SnO_2/C displayed no obvious change before and after 3000 cyclic voltammetry (CV) cycles. The electrocatalytic stability of Ru SAs-SnO_2/C was further tested at an overpotential of −0.018 V by the long-term chronoamperometry. The inset in Figure 4e showed that the current density of Ru SAs-SnO_2/C was maintained well after 27 h. In contrast, the current density of commercial Pt/C showed a drop of 35 % (Figure S20, Supporting Information). In addition, we investigated the stability of Ru SAs-SnO_2/C at a higher overpotential (−0.11 V), no significant current loss was observed after 27 h, indicating excellent stability during the process of HER (Figure S21, Supporting Information). Furthermore, the composition of Ru SAs-SnO_2/C after durability tests was studied by XRD and XPS; no obvious change was found in the structure and chemical composition (Figures S22–S24, Supporting Information).

Owing to its excellent HER activity, an alkaline electrolyzer was assembled using Ru SAs-SnO_2/C as cathode and commercial RuO_2 as anode. As shown in Figure 4f, the Ru SAs-SnO_2/C||RuO_2 couple required only 1.49 V to achieve a current density of 10 $mA cm^{-2}$, lower than that of Pt/C||RuO_2 couple (1.55 V at 10 $mA cm^{-2}$). Furthermore, the current density of Ru SAs-SnO_2/C||RuO_2 couple was obviously higher than that of Pt/C||RuO_2 couple at large voltages. In addition, we also evaluated the stability of the assembled Ru SAs-SnO_2/C||IrO_2 couple. As shown in Figure S25 (Supporting Information), the reduction of current density was negligible over 27 h water electrolysis. The Faradaic efficiency for HER was evaluated by the water drainage method, which exhibited nearly 100 % Faradaic efficiency (Figure S26, Supporting Information).

Understanding the Active Centers

To get insights into the active sites on Ru SAs-SnO_2/C, thiocyanate ions (SCN^-) were added to the electrolyte, which was considered as a poisoner of metal-centered active sites. As depicted in Figure S27 (Supporting Information), the current density of Ru SAs-SnO_2/C decreased from 10.8 to 0.5 $mA cm^{-2}$, indicating the blocking of Ru active sites. To gain deeper insights about the excellent HER activity of Ru SAs-SnO_2/C, the CVs of Ru SAs-SnO_2/C and Ru/C were used to explore their interaction with OH_{ad} in 1.0 M KOH. As shown in Figure 5a, the OH-adsorption (OH_{ad} region: $0.60 < E < 1.00$ V) onset and peak potential of Ru SAs-SnO_2/C displayed a negative shift compared to that of Ru/C and SnO_2/C, confirming stronger oxophilicity of SnO_2 over that of single Ru atoms.[19] The larger current range of Ru SAs-SnO_2/C could be ascribed to its larger ECSA, which results in a large double layer capacitance (Figure S17, Supporting Information). In addition, CO oxidation experiment has been performed to evaluate the OH adsorption capacity. Because the Ru SAs-SnO_2/C and Ru/C didn't show a strong ability to adsorb CO, the Pt black was mixed with our samples to evaluate their OH adsorption capacity (Figure S28, Supporting Information). The onset and peak potentials for CO oxidation on Ru SAs-SnO_2/C + Pt black showed observed negative shifts compared with those of and Ru/C + Pt black and Pt black, respectively. For the onset potential of Ru SAs-SnO_2/C + Pt black, it displayed a 36 mV and 70 mV of negative shift compared to those of Ru/C + Pt black and Pt black, respectively. Meanwhile, the peak potential of Ru SAs-SnO_2/C + Pt black exhibited a negative shift of 7 mV and 15 mV compared to those of Ru/C + Pt black and Pt black, respectively. The enhanced anti-poisoning ability for CO could be attributed to the formation of SnO_2-OH and Ru-OH, which were able to oxidize the CO adsorbed on the Pt active sites at a lower potential. Obviously, Ru SAs-SnO_2/C + Pt black displayed the best CO anti-poisoning ability among the three samples, indicating that SnO_2 species owns the better ability of OH-adsorption than that of Ru species. Zeta potential was used to assess the chargeability of the catalyst surface. As displayed in Figure S29b, the Ru/C owned a more negative potential than that of Ru SAs-SnO_2/C in 1.0 M KOH. The slightly negative surface charge on the Ru SAs-SnO_2/C indicated that the strong adsorption strength between adsorption site and OH_{ad} hindered the OH_{ad} transfer process ($OH_{ad} + e^- \rightleftharpoons OH^-$).[3] The above tests were performed to evaluate their ability for OH-adsorption under positive potential and without external voltage. Based on results, we demonstrated that the OH-adsorption capacity of SnO_2 was significantly stronger than that of Ru. Given this, we also reasonably speculate that SnO_2 owns better OH-adsorption capacity than that of Ru under negative potential. Hence, the competitive adsorption of OH between Ru and SnO_2 reduced the formation of Ru-OH_{ad}, which effectively alleviated the poisoning of Ru sites and improved the HER activity.

DFT calculations were further performed to elucidate the effect of Ru single-atom incorporation into SnO_2 on its structural and HER performance. According to the experimental characterization, a model of atomic Ru doped on the SnO_2 cluster (Ru SAs/SnO_2) was constructed. The structural parameters of the established model are well

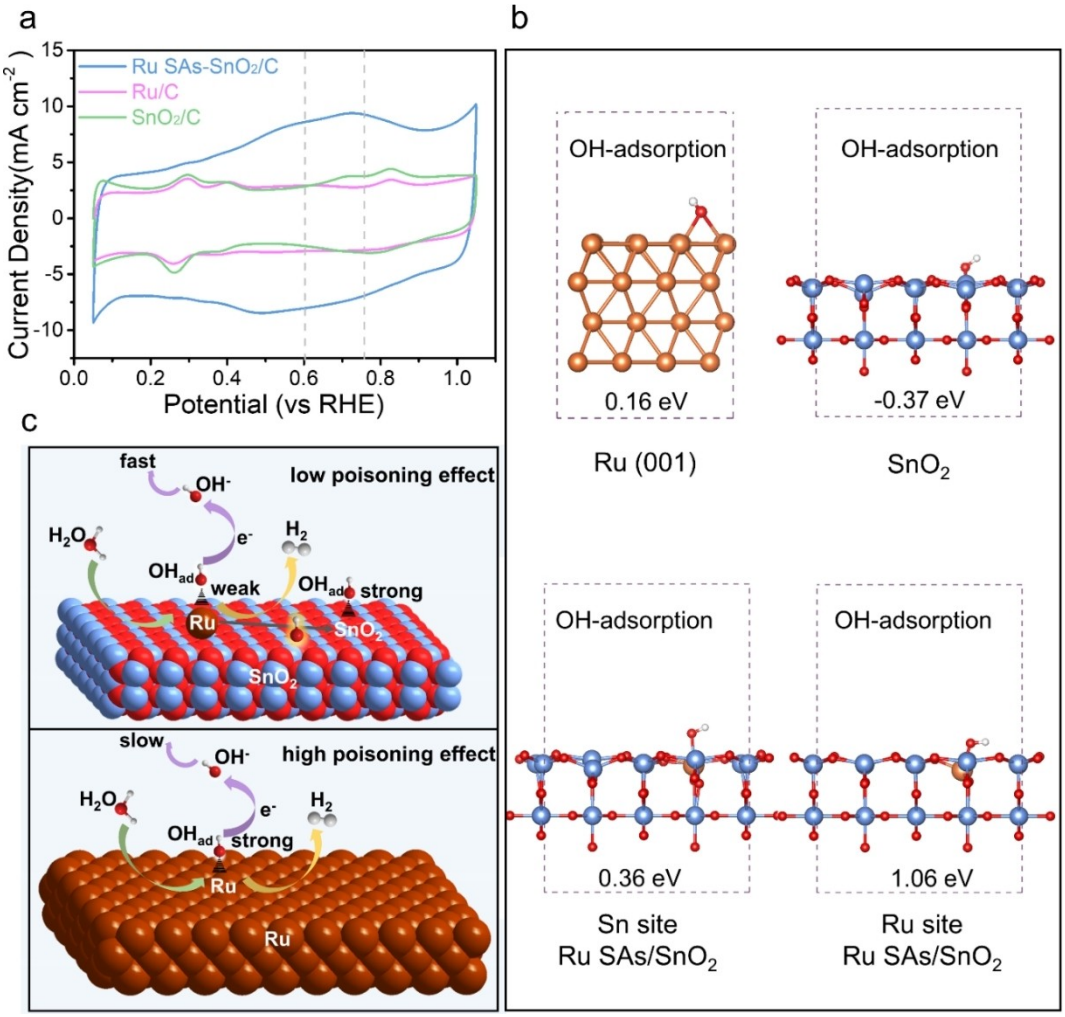

Figure 5. a) CVs curves of Ru SAs-SnO_2/C, Ru/C and SnO_2/C in 1.0 M KOH. OH adsorption configurations on the b) Ru (001), Ru site on Ru SAs/SnO_2 and Sn site on Ru SAs/SnO_2, as well as corresponding binding energies. c) Schematic showing of the mechanism of enhanced HER activity on Ru SAs-SnO_2/C.

consistent with the experimental analysis (Figure S30 and Table S2). In addition, the structures of Pt (111), Ru (001), and pristine SnO_2 were also established (Figure S31, Supporting Information). The differential charge densities of Ru SAs/SnO_2 is simulated to investigate its electronic structure (Figure S32, Supporting Information). There is an obvious charge accumulation around the single-atom Ru site, indicating the electron transfer occurs between Ru and O. The direction of electron transfer is from Ru to O, which decreases the d-band filling of Ru decreases, weakening the strong H-absorption.

From the thermodynamic aspect, the binding energies of OH on Ru (001), bare SnO_2, and Ru SAs/SnO_2 were first calculated. As shown in Figure 5b, OH_{ad} is more favorably adsorbed on the SnO_2 (−0.37 eV) than that of Ru (001) (0.16 eV). When the Ru atoms are stabilized on the surface of SnO_2, the binding energy of OH_{ad} on Ru sites (1.06 eV) exhibits a weaker interaction with OH_{ad} than that of Sn sites (0.36 eV). Hence, for the Ru SAs/SnO_2, it can be rationally deduced that OH adsorbs preferentially on SnO_2, which effectively alleviates the poisoning of Ru sites, facilitating the OH_{ad} transfer process ($OH_{ad}+e^- \rightleftharpoons OH^-$) and the regeneration of Ru active sites (Figure 5c).

Generally, during alkaline HER, H_2O-adsorption, H_2O-dissociation, and H-recombination occurred (Figure 6a). Thus, a strong M-H_2O binding energy, a high efficiency on H_2O-dissociation, and an optimized H-adsorption free energy are desired for the excellent HER activity. The adsorption energy of H_2O on Pt (111), Ru (001), bare SnO_2, and Ru SAs/SnO_2 were firstly calculated (Figure S33, Supporting Information). The results shows that Ru site on Ru SAs/SnO_2 displays much lower adsorption energy of H_2O (the H_2O-adsorption free energy: $\Delta G_{H_2O*} = -1.19$ eV) compared with that of Pt (111), Ru (001), bare SnO_2 and Sn site on Ru SAs/SnO_2, indicating the fastest H_2O-adsorption, which accelerates the following step to dissociate H_2O. Next, their structures for H_2O-dissociation were established. As shown in Figure 6b and Figure S34, compared with Pt (111), Ru (001), bare SnO_2, and Sn site on Ru SAs/SnO_2, the Ru sites on Ru SAs/SnO_2 presents the best H_2O-dissociation

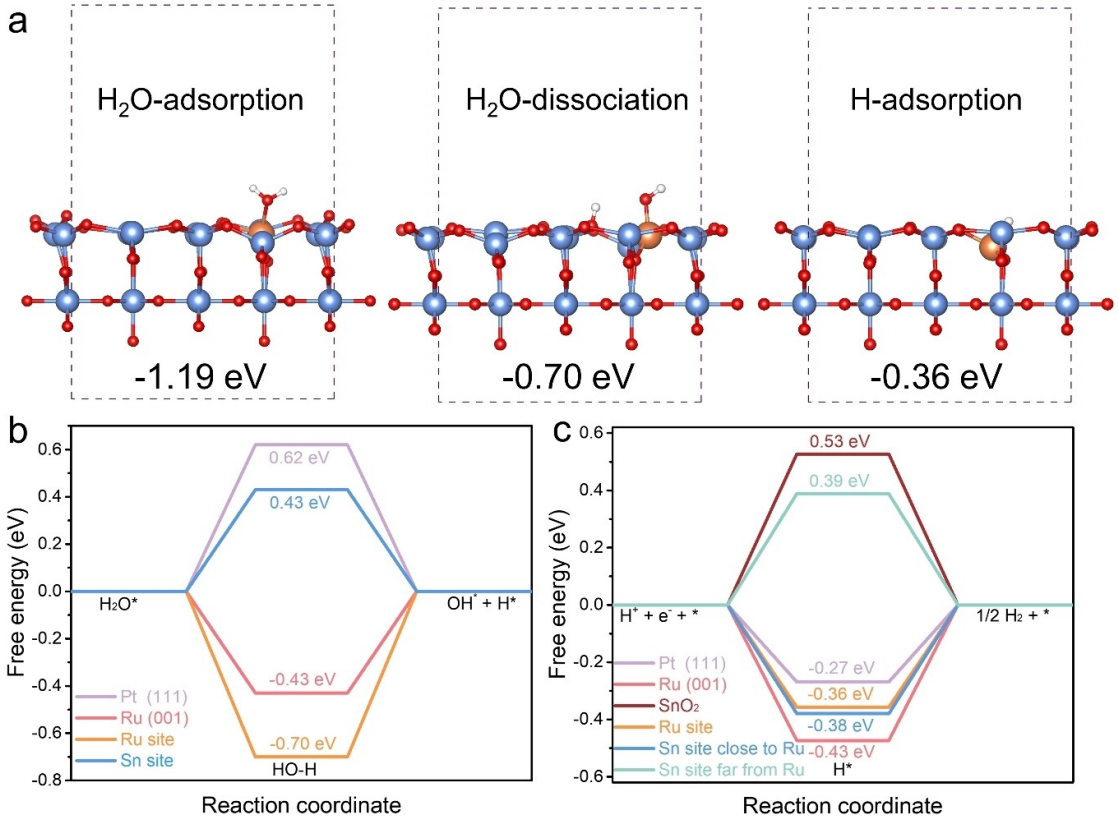

Figure 6. a) Calculated free energies of H_2O-adsorption, H_2O-dissociation, and H-adsorption on Ru SAs/SnO_2. b) Calculated free energies for H_2O-dissociation on different sites. c) Calculated free energies for H-adsorption on different sites.

ability (−0.7 eV), manifesting the faster proton supply. Finally, the H-adsorption free energy (ΔG_{H^*}) is achieved (Figure S35, Supporting Information), Pt (111) processed the optimum ΔG_{H^*} value of −0.27 eV. As a comparison, the ΔG_{H^*} value of Ru (001), bare SnO_2, and Ru/SnO_2 are also calculated. Ru (001) exhibits a more negative ΔG_{H^*} value of −0.43 eV, indicating excessive strong adsorption of H, which impedes the desorption of H. For the model of Ru/SnO_2, the ΔG_{H^*} value of Ru sites is −0.36 eV, suggesting the optimized Ru–H binding energy. In addition, the Sn–H binding energy (close to the Ru sites) is also improved. In contrast, the Sn–H binding energy of Sn (far from the Ru site) (0.39 eV) and bare SnO_2 (0.53 eV) are much weaker (Figure 6c). It is proved that Ru also improved the ability of H-adsorption on Sn site nearby and facilitated the HER process.

Based on the above results, the outstanding HER activity of Ru SAs-SnO_2/C originated from the following points: Firstly, owing to the fast OH_{ad} transfer, the H_2O-dissociation ability of Ru was enhanced, which provided faster proton supply. Secondly, the SnO_2 acted as the competitor to relieve the poisoning effect of Ru-OH_{ad}, facilitating the OH_{ad} transfer process and the regeneration of Ru active sites, which provided more active sites for the re-adsorption of H_2O and H. Thirdly, the sync boosting of the water dissociation and H-adsorption on the single Ru site on SnO_2 enhanced the HER activity. For Pt (111), although it owned the optimal H_{ad}, it displayed the highest water dissociation barrier, resulting into its poorer HER performance than that of Ru SAs-SnO_2/C.

Conclusion

In summary, we demonstrated a competitive adsorption strategy to relieve the strong Ru-OH_{ad} binding energies by introducing another oxophilic species SnO_2, which regulated the strong interaction between Ru and OH_{ad}. Both experimental results and DFT calculation unveiled that the competitive adsorption of OH_{ad} between Ru and SnO_2 facilitated the OH_{ad} transfer process ($OH_{ad} + e^- \rightleftharpoons OH^-$), which effectively alleviated the poisoning of Ru sites and accelerated the regeneration of Ru active sites. The achieved Ru SAs-SnO_2/C displayed an ultralow overpotential of 10 mV at 10 mA cm^{-2} and low Tafel slope of 25 mV dec^{-1}, outperforming the commercial Pt/C catalyst in both performance and price (1/3 of Pt). More importantly, the competitive adsorption strategy described in this article to regulate the adsorption strength of intermediates on active sites can also be adopted to explore for other catalytic reactions, such as such as CO_2 reduction and N_2 reduction.

Acknowledgements

We acknowledge financial support from the Jiangsu Specially Appointed Professorship, the National Key R&D Program of China (2021YFA1502700), the Natural Science Foundation of Jiangsu Province (Grant No. BK20220369), the European Union's Horizon 2020 research and innovation programme (GrapheneCore3: 881603), Deutsche Forschungsgemeinschaft within the Cluster of Excellence, and CRC 1415 (Grant No. 417590517). Open Access funding enabled and organized by Projekt DEAL.

Conflict of Interest

The authors declare no conflict of interest.

Data Availability Statement

The data that support the findings of this study are available from the corresponding author upon reasonable request.

Keywords: Competitive Adsorption · Hydrogen Evolution Reaction · OH_{ad} Transfer Process · Poisoning Effect · Ru Single-Atom

[1] a) Y. Liu, X. Li, Q. Zhang, W. Li, Y. Xie, H. Liu, L. Shang, Z. Liu, Z. Chen, L. Gu, Z. Tang, T. Zhang, S. Lu, *Angew. Chem. Int. Ed.* **2020**, *59*, 1718–1726; *Angew. Chem.* **2020**, *132*, 1735–1743; b) H. Song, M. Wu, Z. Tang, J. S. Tse, B. Yang, S. Lu, *Angew. Chem. Int. Ed.* **2021**, *60*, 7234–7244; *Angew. Chem.* **2021**, *133*, 7310–7320; c) Y. Sun, Z. Xue, Q. Liu, Y. Jia, Y. Li, K. Liu, Y. Lin, M. Liu, G. Li, C. Y. Su, *Nat. Commun.* **2021**, *12*, 1369; d) W. Ni, T. Wang, P. A. Schouwink, Y. C. Chuang, H. M. Chen, X. Hu, *Angew. Chem. Int. Ed.* **2020**, *59*, 10797–10801; *Angew. Chem.* **2020**, *132*, 10889–10893.

[2] a) Y. Zheng, Y. Jiao, A. Vasileff, S. Z. Qiao, *Angew. Chem. Int. Ed.* **2018**, *57*, 7568–7579; *Angew. Chem.* **2018**, *130*, 7690–7702; b) J. Duan, S. Chen, C. A. Ortiz-Ledon, M. Jaroniec, S. Z. Qiao, *Angew. Chem. Int. Ed.* **2020**, *59*, 8181–8186; *Angew. Chem.* **2020**, *132*, 8258–8263.

[3] B. Mao, P. Sun, Y. Jiang, T. Meng, D. Guo, J. Qin, M. Cao, *Angew. Chem. Int. Ed.* **2020**, *59*, 15232–15237; *Angew. Chem.* **2020**, *132*, 15344–15349.

[4] a) J. Mahmood, F. Li, S. M. Jung, M. S. Okyay, I. Ahmad, S. J. Kim, N. Park, H. Y. Jeong, J. B. Baek, *Nat. Nanotechnol.* **2017**, *12*, 441–446; b) J. Zhu, L. Hu, P. Zhao, L. Y. S. Lee, K. Y. Wong, *Chem. Rev.* **2020**, *120*, 851–918.

[5] D. H. Kweon, M. S. Okyay, S. J. Kim, J. P. Jeon, H. J. Noh, N. Park, J. Mahmood, J. B. Baek, *Nat. Commun.* **2020**, *11*, 1278.

[6] C. H. Chen, D. Wu, Z. Li, R. Zhang, C. G. Kuai, X. R. Zhao, C. K. Dong, S. Z. Qiao, H. Liu, X. W. Du, *Adv. Energy Mater.* **2019**, *9*, 1803913.

[7] H. Zhang, W. Zhou, X. F. Lu, T. Chen, X. W. Lou, *Adv. Energy Mater.* **2020**, *10*, 2000882.

[8] J. Kim, H. Jung, S. M. Jung, J. Hwang, D. Y. Kim, N. Lee, K. S. Kim, H. Kwon, Y. T. Kim, J. W. Han, J. K. Kim, *J. Am. Chem. Soc.* **2021**, *143*, 1399–1408.

[9] a) W. Li, Y. Zhao, Y. Liu, M. Sun, G. I. N. Waterhouse, B. Huang, K. Zhang, T. Zhang, S. Lu, *Angew. Chem. Int. Ed.* **2021**, *60*, 3290–3298; *Angew. Chem.* **2021**, *133*, 3327–3335; b) C. Cai, K. Liu, Y. Zhu, P. Li, Q. Wang, B. Liu, S. Chen, H. Li, L. Zhu, H. Li, J. Fu, Y. Chen, E. Pensa, J. Hu, Y. R. Lu, T. S. Chan, E. Cortés, M. Liu, *Angew. Chem. Int. Ed.* **2022**, *61*, e202113664; *Angew. Chem.* **2022**, *134*, e202113664; c) Y. Zheng, Y. Jiao, Y. Zhu, L. H. Li, Y. Han, Y. Chen, M. Jaroniec, S. Z. Qiao, *J. Am. Chem. Soc.* **2016**, *138*, 16174–16181.

[10] a) Z. Wang, B. Xiao, Z. Lin, Y. Xu, Y. Lin, F. Meng, Q. Zhang, L. Gu, B. Fang, S. Guo, W. Zhong, *Angew. Chem. Int. Ed.* **2021**, *60*, 23388–23393; *Angew. Chem.* **2021**, *133*, 23576–23581; b) C. Li, Z. Chen, H. Yi, Y. Cao, L. Du, Y. Hu, F. Kong, R. Kramer Campen, Y. Gao, C. Du, G. Yin, I. Y. Zhang, Y. Tong, *Angew. Chem. Int. Ed.* **2020**, *59*, 15902–15907; *Angew. Chem.* **2020**, *132*, 16036–16041; c) K. Jiang, M. Luo, Z. Liu, M. Peng, D. Chen, Y. R. Lu, T. S. Chan, F. M. F. de Groot, Y. Tan, *Nat. Commun.* **2021**, *12*, 1687; d) L. Li, L. Bu, B. Huang, P. Wang, C. Shen, S. Bai, T. S. Chan, Q. Shao, Z. Hu, X. Huang, *Adv. Mater.* **2021**, *33*, 2105308.

[11] a) A. Zhang, Y. Liang, H. Zhang, Z. Geng, J. Zeng, *Chem. Soc. Rev.* **2021**, *50*, 9817–9844; b) Q. Wang, X. Huang, Z. L. Zhao, M. Wang, B. Xiang, J. Li, Z. Feng, H. Xu, M. Gu, *J. Am. Chem. Soc.* **2020**, *142*, 7425–7433; c) B. Qiao, A. Wang, X. Yang, L. F. Allard, Z. Jiang, Y. Cui, J. Liu, J. Li, T. Zhang, *Nat. Chem.* **2011**, *3*, 634–641; d) J. Wan, W. Chen, C. Jia, L. Zheng, J. Dong, X. Zheng, Y. Wang, W. Yan, C. Chen, Q. Peng, D. Wang, Y. Li, *Adv. Mater.* **2018**, *30*, 1800047.

[12] Q. He, D. Tian, H. Jiang, D. Cao, S. Wei, D. Liu, P. Song, Y. Lin, L. Song, *Adv. Mater.* **2020**, *32*, 1906972.

[13] X. Chen, J. Wan, J. Wang, Q. Zhang, L. Gu, L. Zheng, N. Wang, R. Yu, *Adv. Mater.* **2021**, *33*, 2104764.

[14] a) P. Li, M. Wang, X. Duan, L. Zheng, X. Cheng, Y. Zhang, Y. Kuang, Y. Li, Q. Ma, Z. Feng, W. Liu, X. Sun, *Nat. Commun.* **2019**, *10*, 1711; b) G. Chen, T. Wang, J. Zhang, P. Liu, H. Sun, X. Zhuang, M. Chen, X. Feng, *Adv. Mater.* **2018**, *30*, 1706279.

[15] T. Y. Chen, G. W. Lee, Y. T. Liu, Y. F. Liao, C. C. Huang, D. S. Lin, T. L. Lin, *J. Mater. Chem. A* **2015**, *3*, 1518–1529.

[16] J. Kim, P. C. Shih, K. C. Tsao, Y. T. Pan, X. Yin, C. J. Sun, H. Yang, *J. Am. Chem. Soc.* **2017**, *139*, 12076–12083.

[17] Y. Chen, P. Wang, H. Hao, J. Hong, H. Li, S. Ji, A. Li, R. Gao, J. Dong, X. Han, M. Liang, D. Wang, Y. Li, *J. Am. Chem. Soc.* **2021**, *143*, 18643–18651.

[18] P. Su, W. Pei, X. Wang, Y. Ma, Q. Jiang, J. Liang, S. Zhou, J. Zhao, J. Liu, G. Q. M. Lu, *Angew. Chem. Int. Ed.* **2021**, *60*, 16044–16050; *Angew. Chem.* **2021**, *133*, 16180–16186.

[19] R. Subbaraman, D. Tripkovic, K. C. Chang, D. Strmcnik, A. P. Paulikas, P. Hirunsit, M. Chan, J. Greeley, V. Stamenkovic, N. M. Markovic, *Nat. Mater.* **2012**, *11*, 550–557.

Manuscript received: June 29, 2022
Accepted manuscript online: July 21, 2022
Version of record online: August 24, 2022